



Scale-Awareness of Light Field Camera Based Visual Odometry

Niclas Zeller^{1,2,3}(✉), Franz Quint², and Uwe Stilla¹

¹ Technische Universität München, Munich, Germany
{niclas.zeller, stilla}@tum.de

² Karlsruhe University of Applied Sciences, Karlsruhe, Germany
franz.quint@hs-karlsruhe.de

³ Visteon, Karlsruhe, Germany

Abstract. We propose a novel direct visual odometry algorithm for micro-lens-array-based light field cameras. The algorithm calculates a detailed, semi-dense 3D point cloud of its environment. This is achieved by establishing probabilistic depth hypotheses based on stereo observations between the micro images of different recordings. Tracking is performed in a coarse-to-fine process, working directly on the recorded raw images. The tracking accounts for changing lighting conditions and utilizes a linear motion model to be more robust. A novel scale optimization framework is proposed. It estimates the scene scale, on the basis of keyframes, and optimizes the scale of the entire trajectory by filtering over multiple estimates. The method is tested based on a versatile dataset consisting of challenging indoor and outdoor sequences and is compared to state-of-the-art monocular and stereo approaches. The algorithm shows the ability to recover the absolute scale of the scene and significantly outperforms state-of-the-art monocular algorithms with respect to scale drifts.

Keywords: Light field · Plenoptic camera · SLAM · Visual odometry

1 Introduction

Over the last years, significant improvements in monocular visual odometry (VO) as well as simultaneous localization and mapping (SLAM) were achieved. Traditionally, the task of tracking a single camera was solved by indirect approaches [1]. These approaches extract a set of geometric interest points from the recorded images and estimate the underlying model parameters (3D point coordinates and camera orientation) based on these points. Recently, it was shown that so-called direct approaches, which work directly on pixel intensities, significantly outperform indirect methods [2]. These newest monocular VO and SLAM approaches succeed in versatile and challenging environments. However, a significant drawback remains for all monocular algorithms, by nature. This is that a pure monocular VO system will never be able to recover the scale of the scene.

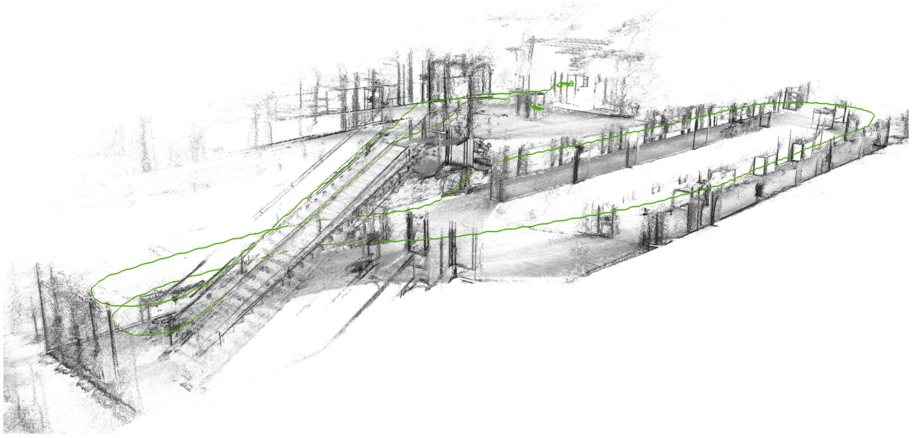


Fig. 1. Example of a point cloud calculated by the proposed Scale-Optimized Plenoptic Odometry (SPO) algorithm. Estimated camera trajectory is shown in green. (Color figure online)

In contrast, a light field camera (or plenoptic camera) is a single-sensor camera which is able to obtain depth from a single image and therefore, can also recover the scale of the scene – at least in theory. Although, the camera still has a size similar to that of a monocular camera.

In this paper, we present Scale-Optimized Plenoptic Odometry (SPO), a completely direct VO algorithm. The algorithm works directly on the raw images recorded by a focused plenoptic camera. It reliably tracks the camera motion and establishes a probabilistic semi-dense 3D point cloud of the environment. At the same time it obtains the absolute scale of the camera trajectory and thus, the scale of the 3D world. Figure 1 shows, by way of example, a 3D map calculated by the algorithm.

1.1 Related Work

Monocular Algorithms. During the last years several indirect (feature-based) and direct VO and SLAM algorithms were published. Indirect approaches split the overall task into two sequential steps. Geometric features are extracted from the images and afterwards the camera position and scene structure are estimated solely based on these features [1, 3, 4].

Direct approaches estimate the camera position and scene structure directly based on pixel intensities [2, 5–8]. This way, all image information can be used for the estimation, instead of only those regions which conform to a certain feature descriptor. In [9] a direct tracking front-end in combination with a feature-based optimization back-end is proposed.

Light Field Based Algorithms. There exist only few VO methods based on light field representations [10–12]. While [10, 11] cannot work directly on the raw data of a plenoptic camera, the method presented in [12] performs tracking and mapping directly on the recorded micro images of a focused plenoptic camera.

Other Algorithms. There exist various methods based on other sensors. These include, e.g. stereo cameras [13–16] and RGB-D sensors [15, 17–19]. However, these are not single sensor systems as the method proposed here.

1.2 Contributions

The proposed Scale-Optimized Plenoptic Odometry (SPO) algorithm adds the following two main contributions to the state of the art:

- A **robust tracking framework**, which is able to accurately track the camera in versatile and challenging environments. Tracking is performed in a coarse-to-fine approach, directly on the recorded micro images. Robustness is achieved by compensating changes in the lighting conditions and performing a weighted Gauss-Newton optimization which is constrained by a linear motion prediction.
- A **scale optimization framework**, which continuously estimates the absolute scale of the scene based on keyframes. It is filtered over multiple estimates to obtain a globally optimized scale. The framework allows to recover the absolute scale and simultaneously scale drifts along the trajectory are significantly reduced.

Furthermore, we evaluated SPO based on a versatile and challenging dataset [20] and compare it to state-of-the-art monocular and stereo VO algorithms.

2 The Focused Plenoptic Camera

In contrast to a monocular camera, a focused plenoptic camera does not only capture a 2D image, but the entire light field of the scene as a 4D function. This is achieved by simply placing a micro lens array (MLA) in front of the image sensor, as it is visualized in Fig. 2(a). The MLA has the effect that multiple micro images are formed on the sensor. These micro images encode both spatial and angular information about the light rays emitted by the scene in front of the camera.

In this paper we will concentrate on so-called focused plenoptic cameras [21, 22]. For this type of camera, each micro image is a focused image which contains a small portion of the entire scene. Neighboring micro images show similar portions from slightly different perspectives (see Fig. 2(b)). Hence, the depth of a certain object point can be recovered from correspondences in the micro images [23]. Furthermore, using this depth, one is able to synthesize the intensities of the so-called virtual image (see Fig. 2(a)) which is created by the main lens [22]. This image is called totally focused (or total focus) image (Fig. 2(c)).

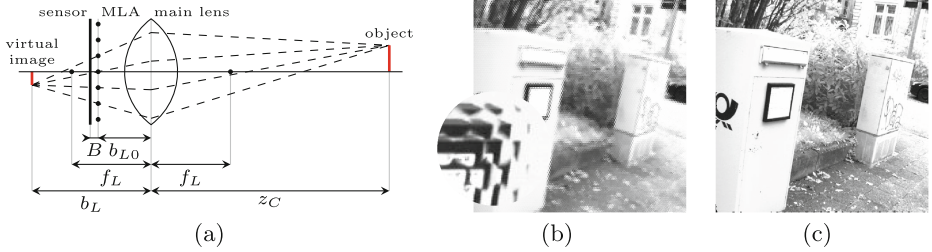


Fig. 2. Focused plenoptic camera. (a) Cross view: the MLA is placed in front of the sensor and creates multiple focused micro images of the same point of the virtual main lens image. (b) Raw image recorded by a focused plenoptic camera. (c) Totally focused image calculated from the raw image. This image is the virtual image.

3 SPO: Scale-Optimized Plenoptic Odometry

Section 3.1 introduces some notations, which will be used in this section. Furthermore, Sect. 3.2 gives an overview of the entire Scale-Optimized Plenoptic Odometry (SPO) algorithm. Afterwards, the main components of the algorithm are presented in detail.

3.1 Notations

In the following, we denote vectors by bold, lower-case letters ξ and matrices by bold, upper case letters G . For vectors defining points we do not differentiate between homogeneous and non-homogeneous representations. However, this should be clear from the context. Frame poses are defined either in $G \in SE(3)$ (3D rigid body transformation) or in $S \in Sim(3)$ (3D similarity transformation):

$$G := \begin{bmatrix} R & t \\ 0 & 1 \end{bmatrix} \quad \text{and} \quad S := \begin{bmatrix} sR & t \\ 0 & 1 \end{bmatrix} \quad \text{with } R \in SO(3), t \in \mathbb{R}^3, s \in \mathbb{R}^+. \quad (1)$$

These transformations are represented by their corresponding tangent space vector of the respective Lie-Algebra. Here, the exponential map and its inverse are denoted as follows:

$$G = \exp_{se(3)}(\xi) \quad \xi = \log_{SE(3)}(G) \quad \text{with } \xi \in \mathbb{R}^6 \text{ and } G \in SE(3), \quad (2)$$

$$S = \exp_{sim(3)}(\xi) \quad \xi = \log_{Sim(3)}(S) \quad \text{with } \xi \in \mathbb{R}^7 \text{ and } S \in Sim(3). \quad (3)$$

3.2 Algorithm Overview

SPO is a direct VO algorithm which uses only the recordings of a focused plenoptic camera to estimate the camera motion and a semi-dense 3D map of the environment. The entire workflow of the algorithm is visualized in Fig. 3 and consists of the following main components:

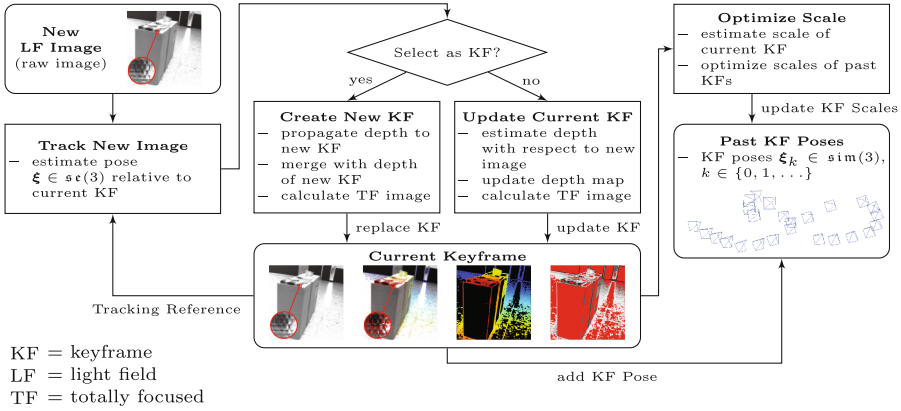


Fig. 3. Flowchart of the Scale-Optimized Plenoptic Odometry (SPO) algorithm.

- New recorded light field images are tracked continuously. Here, the pose $\xi \in \mathfrak{se}(3)$ of the new image, relative to the current keyframe, is estimated. The tracking is constrained by a linear motion model and accounts for changing lighting conditions.
- In addition to its raw light field image, for each keyframe two depth maps (a micro image depth map (used for mapping) and a virtual image depth map (used for tracking)) as well as a totally focused intensity image are stored (see Fig. 5). While depth can be estimated from a single light field image already, the depth maps are gradually refined based on stereo observations, which are obtained with respect to the newly tracked images.
- A scale optimization framework estimates the absolute scale for every replaced keyframe. By filtering over multiple scale estimates a globally optimized scale is obtained. The poses of past keyframes are stored as 3D similarity transformations ($\xi_k \in \mathfrak{sim}(3), k \in \{0, 1, \dots\}$). This way, their scales can simply be updated.

Due to lacking depth information, the initialization is always an issue for monocular VO. This is not the case for SPO, as depth can be obtained for the first recorded image already.

3.3 Camera Model and Calibration

In [12], a new model for plenoptic cameras was proposed. This model is visualized in Fig. 4(a). Here, the plenoptic camera is represented as a virtual array of cameras with a very narrow field of view, at a distance z_{C0} to the main lens:

$$z_{C0} = \frac{f_L \cdot b_{L0}}{f_L - b_{L0}}. \tag{4}$$

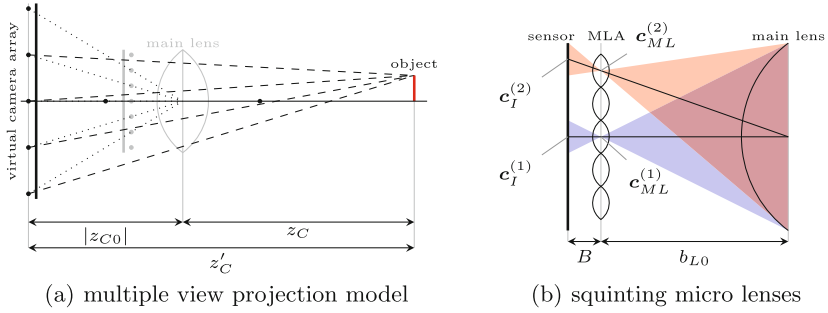


Fig. 4. Plenoptic camera model used in SPO. (a) The model of a focused plenoptic camera proposed in [12]. As shown in the figure, a plenoptic camera forms, in fact, the equivalent to a virtual array of cameras with a very narrow field of view. (b) Squinting micro lenses in a plenoptic camera. It is very often claimed that micro image centers c_I which can be estimated from a white image recorded by the plenoptic camera would be equivalent to the centers c_{ML} of the micro lenses in the MLA. This, in fact, is not the case as micro lenses distant from the optical axis squint, as it is shown in the figure.

In Eq. (4) f_L is the focal length of the main lens and b_{L0} the distance between main lens and real MLA. As this model forms the equivalent to a standard camera array, stereo correspondences between light field images from different perspectives can be found directly in the recorded micro images.

In this model, the relationship between regular 3D camera coordinates $\mathbf{x}_C = [x_C, y_C, z_C]^T$ of an object point and the homogeneous coordinates $\mathbf{x}_p = [x_p, y_p, 1]^T$ of the corresponding 2D point in the image of a virtual camera (or projected micro lens) is given as follows:

$$\mathbf{x}_C := z'_C \cdot \mathbf{x}_p + \mathbf{p}_{ML} = \mathbf{x}'_C + \mathbf{p}_{ML}. \quad (5)$$

In Eq. (5), $\mathbf{p}_{ML} = [p_{MLx}, p_{MLy}, -z_{C0}]^T$ is the optical center of a specific virtual camera. The vector $\mathbf{x}'_C = [x'_C, y'_C, z'_C]^T$ represents the so-called effective camera coordinates of the object point. Effective camera coordinates have their origin in the respective virtual camera center \mathbf{p}_{ML} . Below, we will rather use the definitions c_{ML} and \mathbf{x}_R for the real micro lens centers and raw image coordinates, respectively, instead of their projected equivalents \mathbf{p}_{ML} and \mathbf{x}_p . However, as the maps from one representation into the other are uniquely defined, we can simply switch between both representation. The definitions of these maps as well as further details about the model can be found in [12].

For SPO, this model is extended by some peculiarities of a real plenoptic camera. As the micro lenses in a real plenoptic camera squint (see Fig. 4(b)), this effect is considered in the camera model. Hence, the relationship between a micro image center c_I , which can be detected from a recorded white image [24], and the corresponding micro lens center c_{ML} is defined as follows:

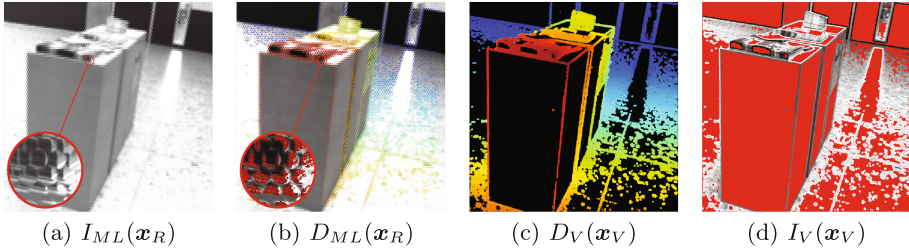


Fig. 5. Intensity images and depth maps stored for each keyframe. (a) Recorded light field image (raw image). (b) Depth map established on raw image coordinates (This depth map is refined in the mapping process). (c) Depth map on virtual image coordinates (This depth map can be calculated from (b) and is used for tracking). (d) Totally focused intensity image (represents intensities of the virtual image). In (d), for the red pixels (black pixels in (c)) no depth value, and therefore no intensity, was calculated.

$$\mathbf{c}_{ML} = \begin{bmatrix} c_{MLx} \\ c_{MLy} \\ b_{L0} \end{bmatrix} = \mathbf{c}_I \frac{b_{L0}}{b_{L0} + B} = \begin{bmatrix} c_{Ix} \\ c_{Iy} \\ b_{L0} + B \end{bmatrix} \frac{b_{L0}}{b_{L0} + B}. \quad (6)$$

Both, \mathbf{c}_I and \mathbf{c}_{ML} are defined as 3D coordinates with their origin in the optical center of the main lens. In addition, we define a standard lens distortion model [25], considering radial symmetric and tangential distortion, directly in the recorded raw image (on raw image coordinates \mathbf{x}_R).

While in this paper the plenoptic camera representation of [12] is used, a similar representation was described in [26].

3.4 Depth Map Representations in Keyframes

SPO establishes for each keyframe two separate representations: one on raw image coordinates \mathbf{x}_R (raw image or micro image representation), and one on virtual image coordinates \mathbf{x}_V (virtual image representation).

Raw Image Representation. The raw intensity image $I_{ML}(\mathbf{x}_R)$ (Fig. 5(a)) is the image which is recorded by the plenoptic camera and consists of thousands of micro images. For each pixel in the image which has a sufficiently high intensity gradient a depth estimate is established and gradually refined based on stereo observations between the keyframe and new tracked frames. This is done in a way similar to [12]. This raw image depth map $D_{ML}(\mathbf{x}_R)$ is shown in Fig. 5(b).

Virtual Image Representation. Between the object space and the raw image representation there exists a one-to-many mapping, as one object point is mapped to multiple micro images. From the raw image representation a virtual image representation, consisting of a depth map $D_V(\mathbf{x}_V)$ in virtual image coordinates (Fig. 5(c)) and the corresponding totally focused intensity image $I_V(\mathbf{x}_V)$

(Fig. 5(d)) can be calculated. Here, raw image points corresponding the same object point are combined and hence, a one-to-one mapping between object and image space is established. The virtual image representation is used to track new images, as will be described in Sect. 3.7.

Probabilistic Depth Model. Rather than representing depths as absolute values, they are represented as probabilistic hypotheses:

$$D(\mathbf{x}) := \mathcal{N}(d, \sigma_d^2), \quad (7)$$

where d defines the inverse effective depth z_C^{-1} of a point in either of the two representations. The depth hypotheses are established in a way similar to [12], where the variance σ_d^2 is calculated based on a disparity error model, which takes multiple error sources into account.

3.5 Final Map Representation

The final 3D map is a collection of virtual image representations as well as the respective keyframe poses combined to a global map. The keyframe poses are a concatenation of 3D similarity transformations $\xi_k \in \mathfrak{sim}(3)$, where the respective scale is optimized by the scale optimization framework (Sect. 3.8).

3.6 Selecting Keyframes

When a tracked image is selected to become a new keyframe, depth estimation is performed in the new image. Afterwards, the raw image depth map of the current keyframe is propagated to the new one and the depth hypotheses are merged.

3.7 Tracking New Light Field Images

For a new recorded frame (index j), its pose $\xi_{kj} \in \mathfrak{se}(3)$, relative to the current keyframe (index k), is estimated by direct image alignment. The problem is solved in a coarse-to-fine approach to increase the region of convergence.

We build pyramid levels of the new recorded raw image $I_{MLj}(\mathbf{x}_R)$ and of the virtual image representation $\{I_{Vk}(\mathbf{x}_V), D_{Vk}(\mathbf{x}_V)\}$ of the current keyframe, by simply binning pixels. As long as the size of a raw image pixel, on a certain pyramid level, is smaller than a micro image, the image of reduced resolution still is a valid light field image. At coarse levels, where the pixel size exceeds the size of a micro image, the raw image turns into a (slightly blurred) central perspective image.

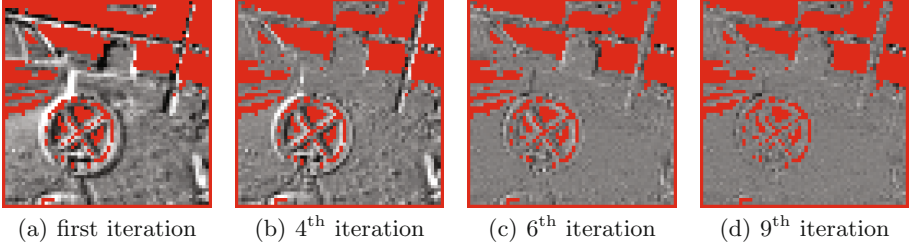


Fig. 6. Tracking residual after various numbers of iterations. The figure shows residuals in virtual image coordinates of the tracking reference. The gray value represents the value of the tracking residual. Black signifies a negative residual with high absolute values and white signifies a positive residual with high absolute value. Red regions are invalid depth pixels and therefore have no residual.

At each of the pyramid levels, a energy function is defined, and optimized with respect to $\xi_{kj} \in \mathfrak{se}(3)$:

$$E(\xi_{kj}) = \sum_i \sum_l \left\| \left(\frac{r^{(i,l)}}{\sigma_r^{(i,l)}} \right) \right\|_{\delta}^2 + \tau \cdot E_{\text{motion}}(\xi_{kj}), \quad (8)$$

$$r^{(i,l)} := I_{V_k}(\mathbf{x}_V^{(i)}) - I_{ML_j} \left(\pi_{ML} \left(\mathbf{G}(\xi_{kj}) \pi_V^{-1}(\mathbf{x}_V^{(i)}), \mathbf{c}_{ML}^{(l)} \right) \right), \quad (9)$$

$$\left(\sigma_r^{(i,l)} \right)^2 := \sigma_n^2 \left(\frac{1}{N_k} + 1 \right) + \left| \frac{\partial r(\mathbf{x}_V, \xi_{kj})}{\partial d(\mathbf{x}_V)} \right|^2 \sigma_d^2(\mathbf{x}_V^{(i)}). \quad (10)$$

Here, $\pi_{ML}(\mathbf{x}_C, \mathbf{c}_{ML})$ defines the projection from camera coordinates \mathbf{x}_C to raw image coordinates \mathbf{x}_R through a certain micro lens \mathbf{c}_{ML} , and $\pi_V^{-1}(\mathbf{x}_V)$ the inverse projection from virtual image coordinates \mathbf{x}_V to camera coordinates \mathbf{x}_C . To calculate \mathbf{x}_C out of \mathbf{x}_V one needed the corresponding depth value $D_V(\mathbf{x}_V)$. A detailed definition of this projection can be found in [27, Eqs. (3)–(6)]. The expression $\| \cdot \|_{\delta}$ is the robust Huber norm [28]. In Eq. (8), the second summand denotes a motion prior term, as it will be defined in Eq. (12). The parameter τ weights the motion prior with respect to the photometric error (first summand). In Eq. (10), the first summand defines the photometric noise on the residual, while the second summand is the geometric noise component, resulting from noise in the depth estimates.

An intensity value $I_{V_k}(\mathbf{x}_V)$ (Eq. (9)) in the virtual image of the keyframe is calculated as the average of multiple (N_k) micro image intensities. Considering the noise in the different micro images to be uncorrelated, the variance of the noise is N_k times smaller than for an intensity value $I_{ML_j}(\mathbf{x}_R)$ in the new raw images. The variance of the sensor noise σ_n^2 is constant over the entire raw image.

Only for the final (finest) pyramid level, a single reference point $\mathbf{x}_V^{(i)}$ is projected to all micro images in the new frame which actually see this point. This is modeled by the sum over l in Eq. (8). This way we are able to implicitly incorporate the parallaxes in the micro images of the new light field image into the

optimization. For all other levels the sum over l is omitted and $\mathbf{x}_V^{(i)}$ is projected only through the closest micro lens $\mathbf{c}_{ML}^{(0)}$. Figure 6 shows the tracking residual for different iterations in the optimization on a coarse pyramid level.

Motion Prior. A motion prior, based on a linear motion model, is used to constrain the optimization. This way, the region of convergence is shifted to an area where the optimal solution is more likely located.

A linear prediction $\tilde{\xi}_{kj} \in \mathfrak{se}(3)$ of ξ_{kj} is obtained from the pose $\xi_{k(j-1)}$ of the previous image as follows:

$$\tilde{\xi}_{kj} = \log_{\text{SE}(3)} \left(\exp_{\mathfrak{se}(3)}(\dot{\xi}_{j-1}) \cdot \exp_{\mathfrak{se}(3)}(\xi_{k(j-1)}) \right). \quad (11)$$

In Eq. (11) $\dot{\xi}_{j-1} \in \mathfrak{se}(3)$ is the motion vector at the previous image.

Using the pose prediction $\tilde{\xi}_{kj}$, we define the motion term $E_{\text{motion}}(\xi_{kj})$ to constrain the tracking:

$$E_{\text{motion}}(\xi_{kj}) = (\delta\xi)^T \delta\xi, \quad \text{with} \\ \delta\xi = \log_{\text{SE}(3)} \left(\exp_{\mathfrak{se}(3)}(\xi_{kj}) \cdot \exp_{\mathfrak{se}(3)}(\tilde{\xi}_{kj})^{-1} \right). \quad (12)$$

For coarse pyramid levels we are very uncertain about the correct frame pose and therefore a high weight τ is chosen in Eq. (8). This weight is decreased as the optimization moves down in the pyramid. On the final level, the weight is set to $\tau = 0$. This way, an error in the motion prediction does not influence the final estimate.

Lighting Compensation. To compensate for changing lighting conditions between the current keyframe and the new image, the residual term defined in Eq. (9) is extended by an affine transformation of the reference intensities $I_{V_k}(\mathbf{x}_V)$:

$$r^{(i,l)} := I_{V_k} \left(\mathbf{x}_V^{(i)} \right) \cdot a + b - I_{ML_j} \left(\pi_{ML} \left(\mathbf{G}(\xi_{kj}) \pi_V^{-1}(\mathbf{x}_V^{(i)}), \mathbf{c}_{ML}^{(l)} \right) \right). \quad (13)$$

The parameters a and b must also be estimated in the optimization process. We initialize the parameters based on first- and second-order statistics calculated from the intensity images $I_{V_k}(\mathbf{x}_V)$ and $I_{ML_j}(\mathbf{x}_R)$ as follows:

$$a_{\text{init}} := \sigma_{I_{ML_j}} / \sigma_{I_{V_k}} \quad \text{and} \quad b_{\text{init}} := \bar{I}_{ML_j} - \bar{I}_{V_k}. \quad (14)$$

In Eq. (14) \bar{I}_{ML_j} and \bar{I}_{V_k} are the average intensity values over the entire images respectively, while $\sigma_{I_{ML_j}}$ and $\sigma_{I_{V_k}}$ are the empirical standard deviations.

3.8 Optimizing the Global Scale

Scale Estimation in Finalized Keyframes. Scale estimation can be viewed as tracking a light field frame based on its own virtual image depth map $D_V(\mathbf{x}_V)$. However, instead of optimizing all pose parameters, a logarithmized scale (log-scale) parameter ρ is optimized. We work on the log-scale ρ to transform the scale $s = e^\rho$, which is applied on 3D camera coordinates \mathbf{x}_C , into a Euclidean space.

As for the tracking approach (Sect. 3.7), an energy function $E(\rho)$ is defined:

$$E(\rho) = \sum_i \sum_{l \neq 0} \left\| \left(\frac{r^{(i,l)}}{\sigma_r} \right)^2 \right\|_\delta, \tag{15}$$

$$r^{(i,l)} := I_{MLk} \left(\pi_{ML} \left(\pi_V^{-1}(\mathbf{x}_V^{(i)}) \cdot e^\rho, \mathbf{c}_{ML}^{(0)} \right) \right) - I_{MLk} \left(\pi_{ML} \left(\pi_V^{-1}(\mathbf{x}_V^{(i)}) \cdot e^\rho, \mathbf{c}_{ML}^{(l)} \right) \right), \tag{16}$$

$$\left(\sigma_r^{(i,l)} \right)^2 := 2\sigma_n^2 + \left| \frac{\partial r^{(i,l)}(\mathbf{x}_V^{(i)}, \rho)}{\partial \sigma_d(\mathbf{x}_V^{(i)})} \right|^2 \sigma_d^2(\mathbf{x}_V^{(i)}). \tag{17}$$

Instead of defining the photometric residual r with respect to the intensities of the totally focused image, the residuals are defined between the centered micro image and all surrounding micro images, which still see the virtual image point $\mathbf{x}_V^{(i)}$. This way, a wrong initial scale, which affects the intensities in the totally focused image, can not negatively affect the optimization.

In conjunction to the log-scale estimate ρ , its variance σ_ρ^2 is calculated:

$$\sigma_\rho^2 = \frac{N}{\sum_{i=0}^{N-1} \sigma_{\rho i}^{-2}} \quad \text{with} \quad \sigma_{\rho i}^2 = \left| \frac{\partial \rho}{\partial d(\mathbf{x}_V^{(i)})} \right|^2 \cdot \sigma_d(\mathbf{x}_V^{(i)})^2. \tag{18}$$

Far points do not contribute to a reliable scale estimate because for these points the ratio between the micro lens stereo baseline and the effective object distance $z'_C = d^{-1}$ becomes negligibly small. Hence, the N points used to define the scale variance are only the closest N points or, in other words, the points with the highest inverse effective depth d .

Scale Optimization. Since refined depth maps are propagated from keyframe to keyframe, the scales of subsequent keyframes are highly correlated and scale drifts between them are marginal. Hence, the estimated log-scale ρ can be filtered over multiple keyframes.

We formulate the following estimator which calculates the filtered log-scale value $\hat{\rho}^{(l)}$ for a certain keyframe with time index l based on a neighborhood of keyframes:

$$\hat{\rho}^{(l)} = \left(\sum_{m=-M}^M \rho^{(m+l)} \cdot \frac{c^{|m|}}{\left(\sigma_\rho^{(m+l)} \right)^2} \right) \cdot \left(\sum_{m=-M}^M \frac{c^{|m|}}{\left(\sigma_\rho^{(m+l)} \right)^2} \right)^{-1}. \tag{19}$$

In Eq. (19), the variable m is the discrete time index in keyframes. The parameter c ($0 \leq c \leq 1$) defines the correlation between subsequent keyframes. Since we consider a high correlation, c will be close to one. While each log-scale estimate $\rho^{(i)}$ ($i \in \{0, 1, \dots, k\}$) is weighted by its inverse variance, estimates of keyframes which are farther from the keyframe of interest (index l) are down weighted by the respective power of c . The parameter M defines the influence length of the filter.

Due to the linearity of the filter, it can be solved recursively, in a way similar to a Kalman filter.

4 Results

Aside from the proposed SPO, there are no light field camera based VO algorithms available which succeed in challenging environments. Same holds true for datasets to evaluate such algorithms. Hence, we compare our method to state-of-the-art monocular and stereo VO approaches based on a new dataset [20].

The dataset presented in [20] contains various synchronized sequences recorded by a plenoptic camera and a stereo camera system, both mounted on a single hand-held platform. The dataset consists of 11 sequences, all recorded at a frame rate of 30 fps. Similar as for the dataset presented in [29], all sequences end in a very large loop, where start and end of the sequence capture the same scene (see Fig. 8). Hence, the accuracies of a VO algorithm can be measured by the accumulated drift over the entire sequence.

SPO is compared to the state-of-the-art in monocular and stereo VO, namely to DSO [2] and ORB-SLAM2 (monocular and stereo version of it) [1, 15]. For ORB-SLAM2, we disabled relocalization and the detection of loop closures to be able to measure the accumulated drift of the algorithm. Figure 7 shows the results with respect to the dataset [20] as cumulative error plots. That is, the ordinate counts the number of sequences for which an algorithm performed better than a value x on the axis of abscissa. The figure shows the absolute scale error d'_s , the scale drift e'_s , and the alignment error e_{align} . All error metrics were calculated as defined in [20].

In comparison to SPO, the stereo algorithm has a much lower absolute scale error. However, the stereo system does also benefit from a much larger stereo baseline. Furthermore, the ground truth scale is obtained on the basis of the stereo data. Hence, the absolute scale error of the stereo system is rather reflecting the accuracy of the ground truth data. SPO is able to estimate the absolute scale with accuracy of 10%, and better, for most of the sequences. The algorithm performs significantly better with scale optimization than without. Regarding the scale drift over the entire sequence, SPO significantly outperforms existing monocular approaches. Regarding the alignment error SPO seems to perform equally well or only slightly worse than DSO [2]. However, the plenoptic images have a field of view which is much smaller than the one of the regular cameras (see [20]). Figure 8 shows, by way of example, two complete trajectories estimated by SPO. Here, the accumulated drift from start to end is clearly visible.

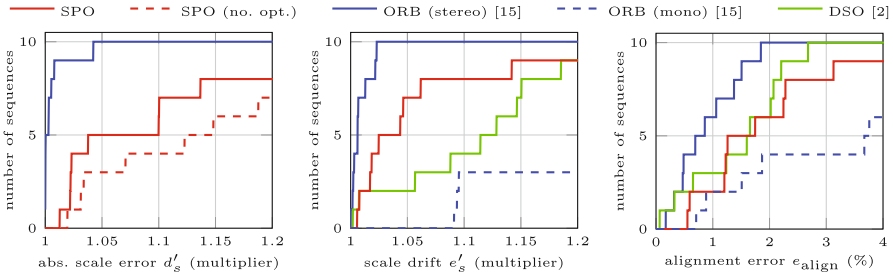


Fig. 7. Cumulative error plots obtained based on the synchronized stereo and plenoptic VO dataset [20]. d'_s and e'_s are multiplicative error, while e_{align} is given in percentages of the sequence length. By nature, no absolute scale error is obtained for the monocular approaches.

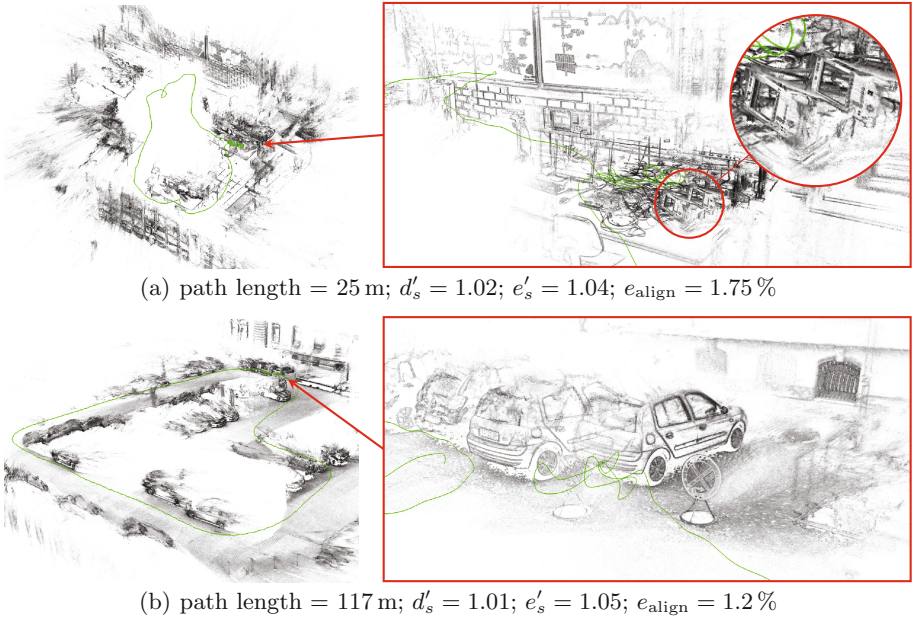


Fig. 8. Point clouds and trajectories calculated by SPO. Left: Entire point cloud and trajectory. Right: Subsection showing beginning and end of the trajectory. In the point clouds on the right the accumulated drift from beginning to end is clearly visible. The estimated camera trajectory is shown in green. (Color figure online)

A major drawback in comparison to monocular approaches is that the focal length of the plenoptic camera can not be chosen freely, but instead directly affects the depth range of the camera. Hence, the plenoptic camera will have a field of view which is always smaller than that of a monocular camera. While this makes tracking more challenging, on the other side it implicates a smaller

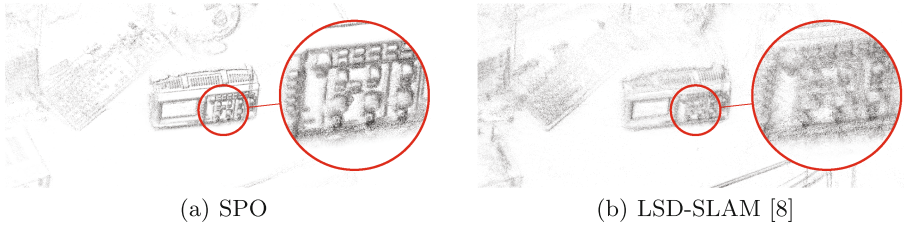


Fig. 9. Point clouds of the same scene: (a) calculated by SPO and (b) calculated by LSD-SLAM. Because of its narrow field of view, the plenoptic camera has much smaller ground sampling distance, which, in turn, results in more detailed 3D map than for the monocular camera. However, as a result the reconstructed map is less complete.

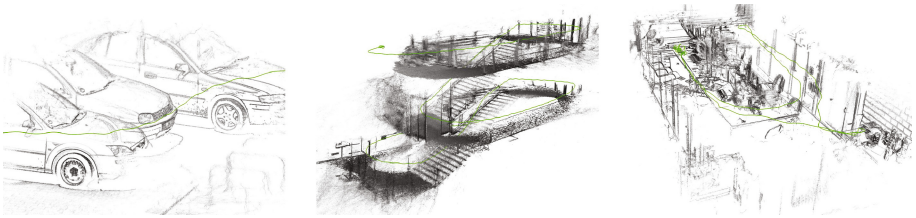


Fig. 10. Examples of point clouds calculated by SPO in various environments. Green line is the estimated camera trajectory. (Color figure online)

ground sampling distance for the plenoptic camera than for the monocular one. Therefore, SPO generally results in point clouds which are more detailed than their monocular (or stereo camera based) equivalent. This can be seen from Fig. 9. Figure 10 shows further results of SPO, demonstrating the quality and versatility of the algorithm.

5 Conclusions

In this paper we presented Scale-Optimized Plenoptic Odometry (SPO), which is a direct and semi-dense VO algorithms working on the recordings of a focused plenoptic camera. In contrast to previous algorithms based on plenoptic cameras and other light field representation [10–12], SPO is able to succeed in challenging real-life scenarios. It was shown that SPO is able to recover the absolute scale of a scene with an accuracy of 10% and better for most of the tested sequences. SPO significantly outperforms state-of-the-art monocular algorithms with respect to scale drifts, while showing similar overall tracking accuracies. In our opinion SPO represents a promising alternative to existing VO and SLAM systems.

Acknowledgment. This research is financed by the Baden-Württemberg Stiftung gGmbH and the Federal Ministry of Education and Research (Germany) in its program FHProfUnt.

References

1. Mur-Artal, R., Montiel, J.M.M., Tardós, J.D.: ORB-SLAM: a versatile and accurate monocular SLAM system. *IEEE Trans. Robot.* **31**(5), 1147–1163 (2015)
2. Engel, J., Koltun, V., Cremers, D.: Direct sparse odometry. *IEEE Trans. Pattern Anal. Mach. Intell.* **40**(3), 611–625 (2018)
3. Klein, G., Murray, D.: Parallel tracking and mapping for small AR workspaces. In: *IEEE and ACM International Symposium on Mixed and Augmented Reality (ISMAR)*, vol. 6, pp. 225–234 (2007)
4. Eade, E., Drummond, T.: Edge landmarks in monocular SLAM. *Image Vis. Comput.* **27**(5), 588–596 (2009)
5. Newcombe, R.A., Lovegrove, S.J., Davison, A.J.: DTAM: dense tracking and mapping in real-time. In: *IEEE International Conference on Computer Vision (ICCV)* (2011)
6. Engel, J., Sturm, J., Cremers, D.: Semi-dense visual odometry for a monocular camera. In: *IEEE International Conference on Computer Vision (ICCV)*, pp. 1449–1456 (2013)
7. Schöps, T., Engel, J., Cremers, D.: Semi-dense visual odometry for AR on a smartphone. In: *IEEE International Symposium on Mixed and Augmented Reality (ISMAR)*, pp. 145–150 (2014)
8. Engel, J., Schöps, T., Cremers, D.: LSD-SLAM: large-scale direct monocular SLAM. In: Fleet, D., Pajdla, T., Schiele, B., Tuytelaars, T. (eds.) *ECCV 2014*. LNCS, vol. 8690, pp. 834–849. Springer, Cham (2014). https://doi.org/10.1007/978-3-319-10605-2_54
9. Forster, C., Pizzoli, M., Scaramuzza, D.: SVO: fast semi-direct monocular visual odometry. In: *IEEE International Conference on Robotics and Automation (ICRA)*, pp. 15–22 (2014)
10. Dansereau, D., Mahon, I., Pizarro, O., Williams, S.: Plenoptic flow: closed-form visual odometry for light field cameras. In: *IEEE/RSJ International Conference on Intelligent Robots and Systems (IROS)*, pp. 4455–4462 (2011)
11. Dong, F., Ieng, S.H., Savatier, X., Etienne-Cummings, R., Benosman, R.: Plenoptic cameras in real-time robotics. *Int. J. Robot. Res.* **32**(2), 206–217 (2013)
12. Zeller, N., Quint, F., Stilla, U.: From the calibration of a light-field camera to direct plenoptic odometry. *IEEE J. Sel. Top. Signal Process.* **11**(7), 1004–1019 (2017)
13. Engel, J., Stücker, J., Cremers, D.: Large-scale direct SLAM with stereo cameras. In: *IEEE/RSJ International Conference on Intelligent Robots and Systems (IROS)*, pp. 1935–1942 (2015)
14. Usenko, V., Engel, J., Stücker, J., Cremers, D.: Direct visual-inertial odometry with stereo cameras. In: *International Conference on Robotics and Automation (ICRA)* (2016)
15. Mur-Artal, R., Tardós, J.D.: ORB-SLAM2: an open-source SLAM system for monocular, stereo, and RGB-D cameras. *IEEE Trans. Robot.* **33**(5), 1255–1262 (2017)
16. Wang, R., Schwörer, M., Cremers, D.: Stereo DSO: large-scale direct sparse visual odometry with stereo cameras. In: *International Conference on Computer Vision (ICCV)* (2017)
17. Izadi, S., et al.: KinectFusion: real-time 3D reconstruction and interaction using a moving depth camera. In: *24th Annual ACM Symposium on User Interface Software and Technology*, pp. 559–568. ACM (2011)

18. Kerl, C., Sturm, J., Cremers, D.: Dense visual SLAM for RGB-D cameras. In: IEEE/RSJ International Conference on Intelligent Robots and Systems (IROS), pp. 2100–2106 (2013)
19. Kerl, C., Stückler, J., Cremers, D.: Dense continuous-time tracking and mapping with rolling shutter RGB-D cameras. In: IEEE International Conference on Computer Vision (ICCV), pp. 2264–2272 (2015)
20. Zeller, N., Quint, F., Stilla, U.: A synchronized stereo and plenoptic visual odometry dataset. [arXiv:1807.09372](https://arxiv.org/abs/1807.09372) (2018)
21. Lumsdaine, A., Georgiev, T.: Full resolution lightfield rendering. Technical report, Adobe Systems, Inc. (2008)
22. Perwaß, C., Wietzke, L.: Single lens 3D-camera with extended depth-of-field. In: SPIE 8291, Human Vision and Electronic Imaging XVII (2012)
23. Zeller, N., Quint, F., Stilla, U.: Establishing a probabilistic depth map from focused plenoptic cameras. In: International Conference on 3D Vision (3DV), pp. 91–99 (2015)
24. Dansereau, D., Pizarro, O., Williams, S.: Decoding, calibration and rectification for lenselet-based plenoptic cameras. In: IEEE Conference on Computer Vision and Pattern Recognition (CVPR), pp. 1027–1034 (2013)
25. Brown, D.C.: Decentering distortion of lenses. *Photogramm. Eng.* **32**(3), 444–462 (1966)
26. Mignard-Debise, L., Restrepo, J., Ihrke, I.: A unifying first-order model for light-field cameras: the equivalent camera array. *IEEE Trans. Comput. Imaging* **3**(4), 798–810 (2017)
27. Zeller, N., Noury, C.A., Quint, F., Teulière, C., Stilla, U., Dhôme, M.: Metric calibration of a focused plenoptic camera based on a 3D calibration target. *ISPRS Ann. Photogramm., Remote. Sens. Spat. Inf. Sci.* **III-3**, 449–456 (2016). (Proceedings of ISPRS Congress 2016)
28. Huber, P.J.: Robust estimation of a location parameter. *Ann. Math. Stat.* **35**(1), 73–101 (1964)
29. Engel, J., Usenko, V., Cremers, D.: A photometrically calibrated benchmark for monocular visual odometry. [arXiv:1607.02555](https://arxiv.org/abs/1607.02555) (2016)